JOURNAL OF AIRCRAFT
Vol. 31, No. 6, November–December 1994

Progress in High-Lift Aerodynamic Calculations

Stuart E. Rogers*
NASA Ames Research Center, Moffett Field, California 94035

The current work presents progress in the effort to numerically simulate the flow over high-lift aerodynamic components, namely multielement airfoils in either a takeoff or landing configuration. The computational approach utilizes an incompressible flow solver and an overlaid chimera grid approach. A detailed grid resolution study is presented for flow over a three-element airfoil. Two turbulence models—a one-equation Baldwin-Barth model and a two-equation k-ω model—are compared. Excellent agreement with experiment is obtained for the lift coefficient at all angles of attack, including the prediction of maximum lift when using the two-equation model. Results for two other flap riggings are shown.

Introduction

THE study of high-lift aerodynamics has become a pacing item in aeronautical design, and thus, tools that can be used to accurately compute this flow are in demand. A computational fluid dynamics (CFD) flow solver to be used for computing high-lift flows needs to be able to accurately, reliably, and efficiently predict changes in aerodynamic performance due to changes in geometry, angle of attack, Mach number, and Reynolds number. This includes predicting maximum lift and computing drag accurately. This is quite a challenge because multielement airfoil flows contain areas with laminar separation, transition, strong adverse pressure gradients, turbulent separation, confluent boundary layers interacting with wakes, and shock/boundary-layer interaction. The payoffs for understanding this flow and designing a more efficient high-lift system for a commercial jet transport are quite high.[1] Increases in lift coefficient and decreases in lift-over-drag can lead to a reduction in the approach attitude, resulting in shorter landing gear and less weight, as well as increases in both payload and range.

Work in developing CFD analysis tools for high-lift systems has been performed by a number of authors.[1-12] The approaches that have been used to numerically solve high-lift flows vary from potential methods coupled with an interactive boundary-layer formulation, to solving the Reynolds-averaged Navier-Stokes equations, using either multizonal structured grids or unstructured grids. As yet, no one has shown the ability to meet all of the goals stated above for a high-lift flow solver, even in two dimensions. The primary shortcomings common to most computational efforts include a lack of adequate grid resolution, inadequate modeling of the turbulence and transition, large computational requirements, and a high degree of complexity that is undesirable in an engineering design environment.

In previous work[13] this author applied an incompressible Navier-Stokes flow solver to a number of multielement airfoil problems using multizonal structured grids. Both a patched grid approach (with pointwise overlap at zonal boundaries) and a chimera overlaid grid approach[14] (with overlapping grids in which the points do not coincide) were used. The chimera grids were found to be easier to use and more flexible, and as a result the chimera grid approach is used in the current work. In the previous work it was found that the computations were fairly accurate, yet some of the details of the flow physics did not agree well with experimental results. These errors primarily involved viscous effects, such as flow separation occurring on the upper surface of the flap. The turbulence model plays a large role in predicting the performance of the airfoil. There are also a number of variables involved with the generation of the overlaid grids that play a role in accurately predicting these flows.

Although an incompressible flow solver will neglect the effects of compressibility, it can simulate most of the low Mach number flows of interest in this area. Experience to date with this approach shows it to be applicable to many high-lift configurations with Mach numbers of 0.2 and below. The superior efficiency of the incompressible formulation will make it a useful research tool in developing the ability to meet the goals stated above. To this end, the current work was initiated with the following goals: 1) investigate the effects of grid resolution on computing the flow over a two-dimensional multielement airfoil, and 2) find a suitable turbulence model for computing this complex flow. These were to be investigated with the underlying constraint that the final approach must be efficient and robust so that it could be utilized in a design environment.

The grid investigation was initiated by first automating the grid generation process for multielement airfoils as much as possible. The effects of the placement of the grid overlap regions and holes were studied to provide guidelines for grid boundary placement. A three-element airfoil was utilized as a test case. A series of grids of varying grid density in the normal and circumferential directions were generated. Computational results using these grids are presented; they provide guidelines on the number of grid points needed to adequately resolve the flow. Two turbulence models (a one-equation Baldwin-Barth model and a two-equation k-ω model) were utilized for all the different grids. This provides ample data for comparing the models. As an additional test, the flow solver is applied to two other cases with different flap positions for the same three-element airfoil, and these results are presented.

Flow Solver

The current computations are performed utilizing the INS2D-UP[15-17] computer codes that solve the incompressible Navier-Stokes equations for both steady-state flows and unsteady computations. The codes are based on the method of artificial compressibility as developed by Chorin,[18] in which a pseudotime derivative of pressure is added to the continuity equa-

Presented as Paper 93-0194 at the AIAA 31st Aerospace Sciences Meeting and Exhibit, Reno, NV, Jan. 11–14, 1993; received Feb. 9, 1993; revision received Jan. 23, 1994; accepted for publication Feb. 1, 1994.

*Aerospace Engineer, Computational Algorithms and Applications Branch, Fluid Dynamics Division, M/S T27B-1. Senior Member AIAA.

tion. Therefore, the convective part of the equations form a hyperbolic system, which can be iterated in pseudotime until a steady-state solution is found. For unsteady problems, subiterations in pseudotime are performed for each physical time step. Since the convective terms of the resulting equations are hyperbolic, upwind differencing can be applied to these terms. The codes use flux-difference splitting based on the scheme of Roe.[19] The upwind differencing leads to a more diagonally dominant system than does central differencing and does not require the use of user-specified artificial dissipation. The system of equations is solved using a Gauss-Seidel type line-relaxation scheme. The line-relaxation scheme is very useful for computing multizonal grids because it makes it possible to iteratively pass ΔQ (which is the change in the dependent variables for one time step) information between the zonal boundaries as the line-relaxation sweeping takes place. The result is a semi-implicit passing of boundary conditions between zones, which further enhances the code stability.[20] The resulting code is very robust and stable. It is capable of producing steady-state solutions to fine-mesh problems in 200–300 iterations.

Turbulence Models

The INS2D-UP flow code has two turbulence models coded with the capability to run multizone, overlaid grids. These models are uncoupled and solved separately from the mean-flow equations. The turbulence model equations are solved using a line-relaxation procedure similar to that used for the mean-flow equations. The field variables for the models are interpolated at the chimera interfaces in the same fashion as the mean-flow variables. The first model is the one-equation model of Baldwin and Barth,[21,22] where the specific formulation found in Ref. 21 is used. It is derived from a simplified form of the standard k-ε model equations. This model has been found to be very robust and easy to implement for multiple-body configurations.

The second turbulence model is a two-equation k-ω model recently developed by Menter[23] for aerodynamic application. It is based on the earlier k-ω model of Wilcox,[24] which was found to perform quite well in comparison with a number of other turbulence models in a study of various adverse pressure gradient flow computations performed by Menter.[25] However, Menter[26] also showed that this model is very sensitive to the specification of freestream values for ω. The current formulation of the model[23] removes the freestream dependency with a zonal approach that automatically switches between the Wilcox model in the near wall region to an equivalent of the k-ε model[27] away from the wall and in free shear layers. In order to improve the sensitivity of the model to adverse pressure gradients, Menter[23] introduced a modification to the definition of the eddy-viscosity that accounts for the transport of the principal turbulent shear stress. The modification is based on Bradshaw's assumption that the principal shear stress is proportional to the turbulent kinetic energy over most of the boundary layer. The model also features terms introduced by Wilcox[28] that allows the prediction of boundary-layer transition without prior knowledge of the transition location. These terms feature two transition specific closure coefficients that have been tuned to accurately predict transition for an incompressible flat-plate boundary layer.

Multielement Airfoils

Recent experimental work has provided detailed measurements for a number of multielement airfoil takeoff and landing configurations.[29,30] The three-element airfoil in a landing configuration is used here as a validation case. The slat and flap are both deflected 30 deg, and the computations are run at a Reynolds number of 9×10^6. The experimental Mach number for the cases used in the current comparison was 0.2. For this configuration, Valarezo et al.[30] showed that the compressibility effects were not significant for freestream Mach numbers less than or equal to 0.2. The experimental results have been corrected for wind-tunnel wall effects, and thus the computations do not include wind-tunnel walls.

Chimera Grid Topology

Experience with the chimera[14] overlaid grid approach has shown that there are a number of different ways to set up the grid interfaces, some of which can cause inaccuracies in the flow solution. A number of these are discussed here following a brief introduction of the chimera interface concept.

The chimera method of domain decomposition allows a system of relatively simple grids, each describing a single component of the computational geometry, to be combined into a composite grid system. The individual grids receive information from each other in the form of interpolated quantities. This communication occurs at two types of boundaries; either a naturally occurring outer boundary of a mesh that overlaps the interior region of another mesh; or at an interior boundary surrounding a hole. The holes are regions of a mesh that are blanked out and computationally ignored since their interior points lie inside a solid body. The points surrounding the holes are known as fringe points and are updated from interpolation information. The job of generating the interpolation stencils and cutting out the holes is performed by the PEGSUS software before the flow code is run. The advantage to using the chimera approach is simplified grid generation. The disadvantage is the introduction of numerical boundary conditions in the interior of the flow domain.

Figure 1 shows the geometry and one of the sets of composite meshes used to study multielement airfoil flow computations. Only every other grid line is shown in this figure. There are four grids in this composite mesh: the first is a c-grid around the slat; number two is a c-grid that resolves the main element and extends to the far field; the third is a c-grid that surrounds the flap; the fourth is an h-grid that covers the flap trailing edge and near wake. This last grid is necessary to resolve the thick trailing edge of the flap. The top of Fig. 1 shows the main element grid; the bottom of the figure shows the other grids. Notice that the inner boundary of the wake of the main-element grid runs parallel to the top surface of the flap. This ensures that the densest region of this grid will resolve the wake of the main element as it flows over and aft of the flap. It also is placed so that the hole caused by the flap will always stay below the wake-cut boundary and avoids the occurrence of a fringe point adjacent to a grid boundary. Notice also that the streamwise spacing of the main-element grid remains nearly constant well aft of the flap. This was found to be necessary in order to resolve the main-element wake and to predict maximum lift conditions. This area is also further resolved by applying an elliptic smoother to the grid spacing in the direction across the wake cut for grid lines aft of the trailing edge. This reduces the aspect ratio of these cells near the wake cut and spreads these grid lines out. This is done for all the c-grids and it results in enhanced convergence.

It can also be seen in Fig. 1 that the normal spacing in the main-element grid is clustered off the body at the position of the slat trailing edge. This type of clustering is also present in the flap grid at the position of the trailing edge of the main element. This was found to be necessary to properly pass the wake from the trailing-edge region of one grid to the recipient

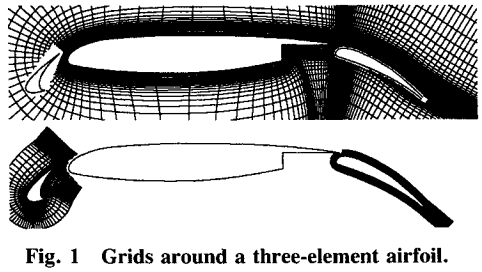

Fig. 1 Grids around a three-element airfoil.

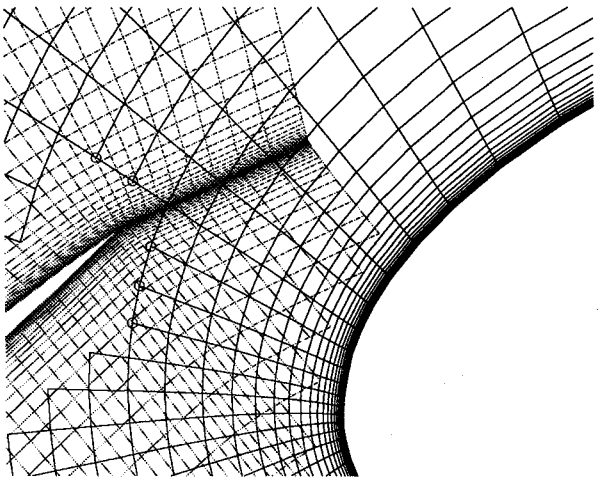

Fig. 2 Previously used grids with poor resolution at slat trailing edge.

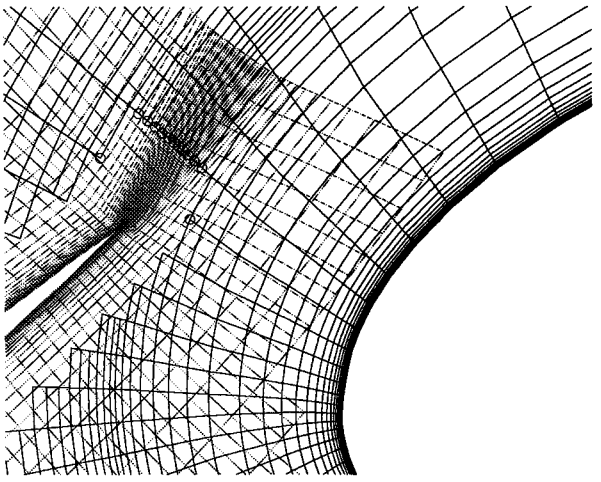

Fig. 3 Grids with enhanced resolution at the slat trailing edge.

grid. Results for the three-element airfoil case reported in the preceding work[13] showed poor agreement in the pressure coefficient on the suction side of the slat, especially for the 8.1-deg angle-of-attack case. The primary cause for this was a lack of resolution of the slat wake. Figure 2 shows the grids from this previous result near the trailing edge of the slat: the hole in the main element grid that receives information from the slat grid is in an area where the main-element grid is very coarse. The grid points denoted with circles are the fringe points. They surround the wake of the slat, but there are no points within the wake. This is remedied by aligning the wake-cut of the slat grid so it is locally parallel with the surface of the main element (and hence parallel with the circumferential grid lines of the main-element grid), and by clustering the main-element grid in the vicinity of the slat trailing edge. This new grid is shown in Fig. 3 where it can be seen that there are many more fringe points lined up across and in the wake.

Figures 4 and 5 show velocity magnitude contours in the vicinity of the slat trailing edge for the old grid and the improved grid, respectively, for an angle of attack of 8.1 deg. Since the old main-element grid did not resolve the wake, it was in turn causing too much mass to flow out of the slat-grid downstream boundary (which is updated by interpolating variables from the main-element grid). Thus, there was too much mass flow over the top of the slat, causing the greater suction.

Grid Resolution Study and Turbulence Models

A grid resolution study was undertaken to quantify the number of grid points necessary to obtain accurate solutions for this multielement airfoil configuration. This was accomplished by generating a series of four grid densities in both the normal and circumferential directions. A series of meshes was generated in which the circumferential grid density was varied while using the finest density in the normal direction. Likewise, meshes that varied the normal grid density used the finest spacings in the circumferential direction. Tables 1 and 2 show the number of points used in each grid component at the different levels of grid density for the variations in the normal and circumferential directions, respectively. Table 1 also lists Δ_w/C, which is the normal spacing at the wall, nondimensionalized by the airfoil chord. Next to the dimension j_{max}, Table 2 also lists the number of points that are on the body for the first three zones. The variable Δ_{TE}/C in Table 2 is the nondimensional streamwise spacing at the trailing edge. The different meshes are denoted by their levels as given in these tables. Thus, grid $n4c4$ uses the finest spacings in both directions, and grid $n1c4$ uses the coarsest normal spacing and the finest circumferential spacing.

Table 1 Normal direction grid densities

	k_{max}				
Level	Slat	Main	Flap	Wake	Δ_w/C
1	21	55	31	81	5.0×10^{-5}
2	31	75	41	111	1.0×10^{-5}
3	41	95	51	141	5.0×10^{-6}
4	51	115	61	171	1.0×10^{-6}

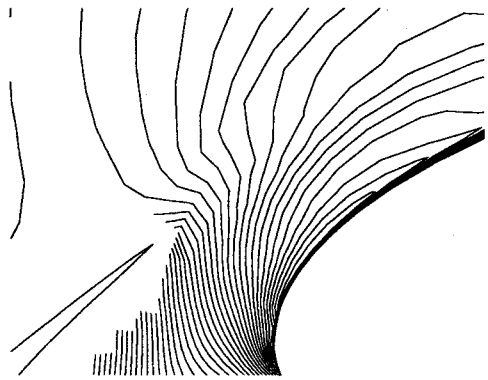

Fig. 4 Velocity magnitude contours with poor slat-wake resolution.

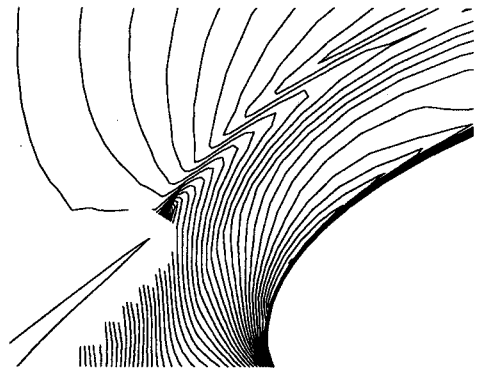

Fig. 5 Velocity magnitude contours with enhanced slat-wake resolution.

The sequences of grid densities result in seven different composite meshes. In order to minimize the change of the chimera interfaces due to changes in the grid resolution, the boundaries that cut the holes in the grids were defined independently of the grid density. Thus the size, shape, and location of the holes does not vary greatly with the grid density. All grid cases were run for seven different angles of attack. This study therefore requires 98 different runs of the code.

In order to properly evaluate each turbulence model, both models were run for all seven composite meshes. The effects

Table 2 Circumferential direction grid densities

Level	j_{max}[a] Slat	Main	Flap	Wake	Δ_{TE}/C
1	121 (101)	261 (101)	105 (101)	11	0.00100
2	161 (121)	341 (141)	125 (121)	21	0.00075
3	201 (141)	421 (181)	145 (141)	31	0.00060
4	241 (161)	501 (221)	165 (161)	41	0.00050

[a]Number of points on body.

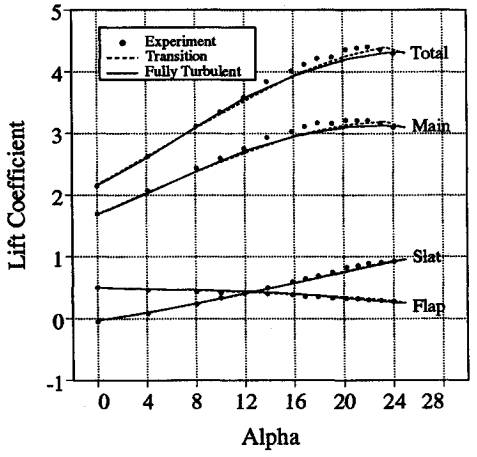

Fig. 6 Lift coefficient vs angle of attack for the k-ω turbulence model with and without transition terms.

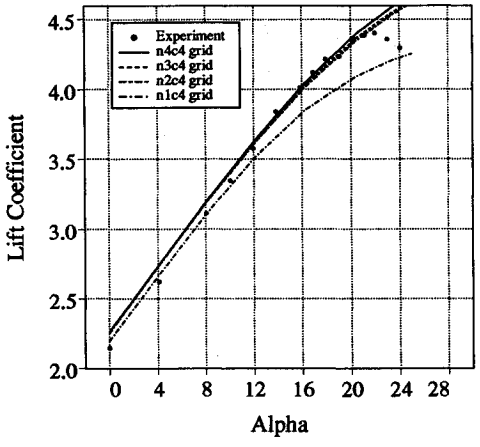

Fig. 7 Lift coefficient vs angle of attack for the Baldwin-Barth turbulence model showing effect of normal grid spacing.

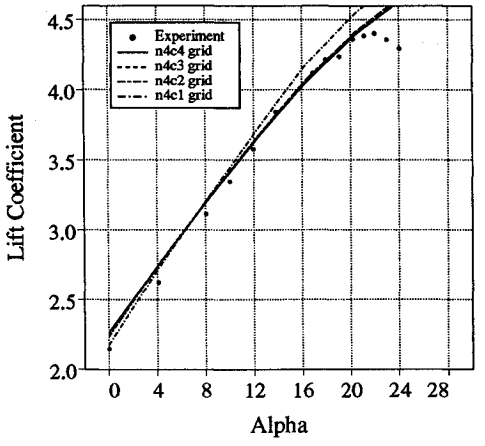

Fig. 8 Lift coefficient vs angle of attack for the Baldwin-Barth turbulence model showing effect of circumferential grid spacing.

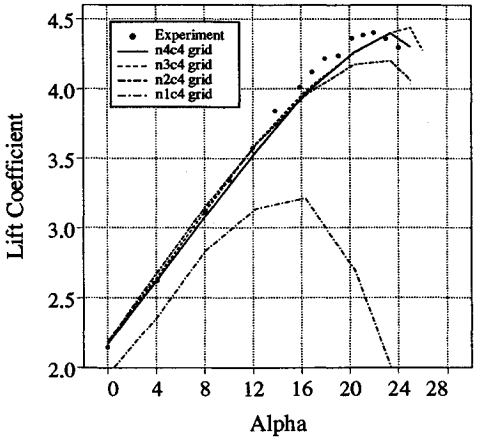

Fig. 9 Lift coefficient vs angle of attack for the k-ω turbulence model showing effect of normal grid spacing.

of transition can be important for multielement airfoil flows. As discussed above, the k-ω model has a transition prediction capability, whereas the Baldwin-Barth model does not have these types of terms implemented. The difference between using free transition vs fully turbulent flow for the k-ω model on the $n4c4$ grid is shown in Fig. 6. The lift coefficient for each of the three elements and the total lift coefficient is plotted vs angle of attack for both cases along with the experimental lift results. The transition does not effect the flow at the lower angles of attack, but it does change the prediction of the maximum lift. In order to provide some consistency between the models in the treatment of transition, the results from the k-ω model with free transition were used to specify the transition location for the Baldwin-Barth computations. This is implemented in the Baldwin-Barth model by turning off the production terms in the model upstream of the transition location.

The results of the grid resolution study for the Baldwin-Barth model are presented in Figs. 7 and 8, which plot the total lift coefficient vs angle of attack. Figure 7 shows the results of the changes in normal spacing, and Fig. 8 shows the variation in the circumferential spacing. Both of these plots show that there is very little difference in the solutions between the second, third, and fourth level of resolution in both directions. This is particularly true at the lower angles of attack. At the highest angles of attack, Fig. 7 shows that the solutions do not converge onto the finest grid solution. These cases were run up to an angle of attack of 25 deg, at this highest angle the Baldwin-Barth calculations had yet to predict stall behavior. Previous results with this model show that it will predict airfoil stall, but usually at angles of attack greater than that measured experimentally.

The grid resolution study results for the k-ω model are shown in Figs. 9 and 10, which plot the total lift coefficient vs angle of attack. The k-ω model shows a much greater dependency on the normal spacing than the previous model. Figure 10 shows that the model has a weaker dependency on the circumferential grid density, because the three finest grid solutions are nearly identical, except that only the finest grid solution agrees with the experimental value for maximum lift. The y^+ values at the first point off the body surface were calculated and averaged for each element. Both turbulence models had very similar values for the given wall grid spacing

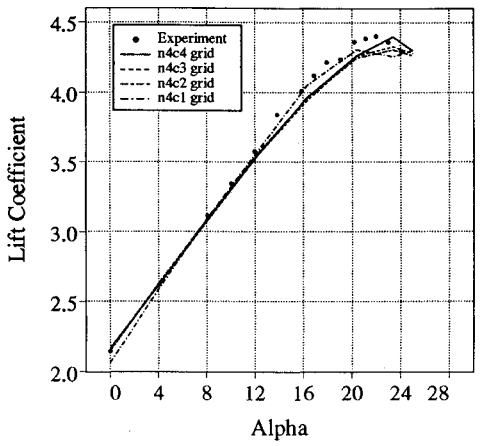

Fig. 10 Lift coefficient vs angle of attack for the k-ω turbulence model showing effect of circumferential grid spacing.

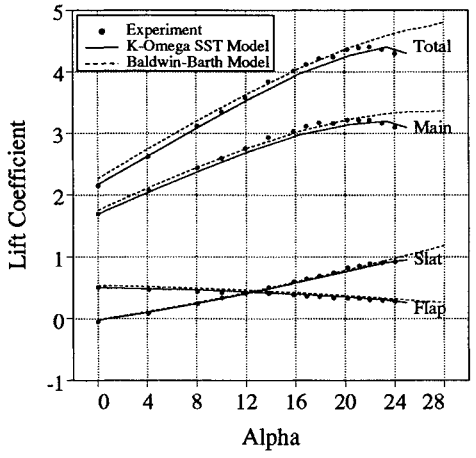

Fig. 11 Lift coefficient vs angle of attack for comparing the Baldwin-Barth and k-ω turbulence models.

at each grid density. This average value of y^+ was approximately 12, 4, 2, and 0.4, for the $n1c4$, $n2c4$, $n3c4$, and $n4c4$ grids, respectively.

In order to compare the difference between the turbulence models, the lift coefficients from the finest grid ($n4c4$) calculations are plotted vs angle of attack in Fig. 11. The most obvious difference in the solutions is the ability of the k-ω model to come very close to predicting maximum lift, where as the Baldwin-Barth model has not stalled even at 28 deg angle of attack. Otherwise, good agreement is seen for both models at the lower angles of attack, with the k-ω having excellent agreement at the lowest angle of attack, but predicting too little lift at the moderate angles, where the Baldwin-Barth model performs quite well. Figure 12 plots the pressure coefficient Cp on the surface of the elements at two different angles of attack comparing both turbulence models against experimental results. Figure 12a shows results from 8.1-deg angle of attack; much of the higher lift from the Baldwin-Barth calculations comes from the slat. Also, this figure shows that the Baldwin-Barth solution does not have a flattening of the Cp at the aft end of the flap upper surface like the experimental results; this flattening is indicative of separation. The k-ω results do show a flattening, but not to the same extent as the experiment. Figure 12b shows the 23.4-deg angle of attack results; both models predict too much lift. At this angle of attack the experimental lift has dropped below maximum lift, while the k-ω predicts maximum lift to occur at this angle.

The biggest drawback of the two-equation model is that it takes more computing time than the one-equation model. This comes from two factors: 1) the two-equation model naturally requires more operations per iteration; and 2) the results of

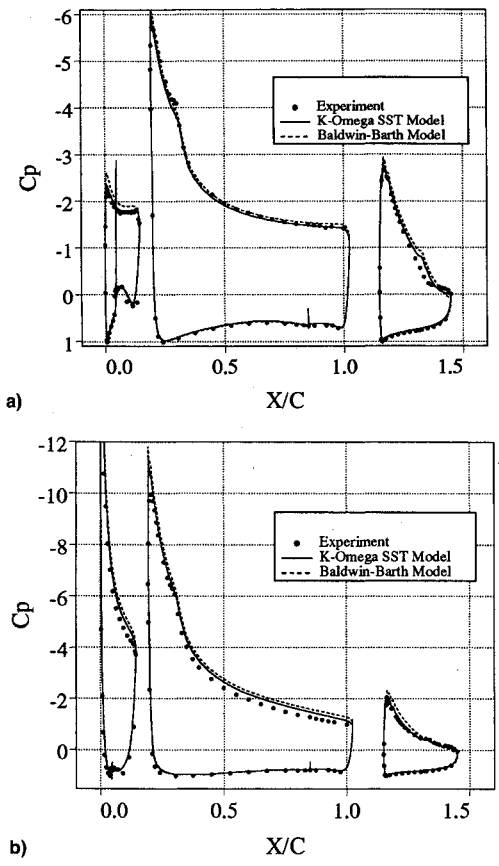

Fig. 12 Pressure coefficient on the airfoil surfaces for the Baldwin-Barth and k-ω turbulence models. Alpha = a) 8.1 and b) 23.4.

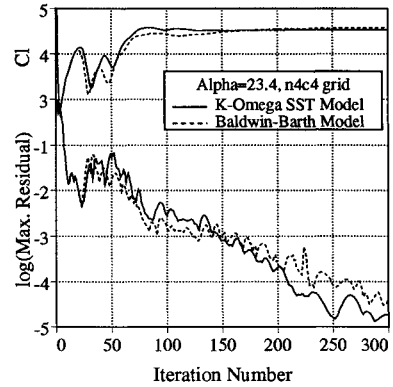

Fig. 13 Convergence histories for the Baldwin-Barth and k-ω turbulence models.

the grid resolution study indicate that the k-ω does require more grid points, especially in the surface-normal direction. The two turbulence models do show very similar convergence properties. Figure 13 plots the maximum residual and the lift coefficient vs iteration number for the finest grid case ($n4c4$) at an angle of attack of 23.4 deg for both of the turbulence models. It can be seen that both models take about 300 iterations for the lift to converge, at which time the residual has dropped about four orders of magnitude. For the finest grid, the code runs on a Cray Y-MP in 5 min/100 iterations for the Baldwin-Barth model, and about 5% slower for the k-ω model.

Since the k-ω model is doing a reasonably good job of predicting the maximum lift for this configuration, it is reasonable to expect that the physics found in the calculated results are representative of the mechanisms responsible for making this multielement airfoil configuration stall. The k-ω results on the finest grid ($n4c4$) are presented in Figs. 14 and 15 where velocity magnitude contours are plotted along with

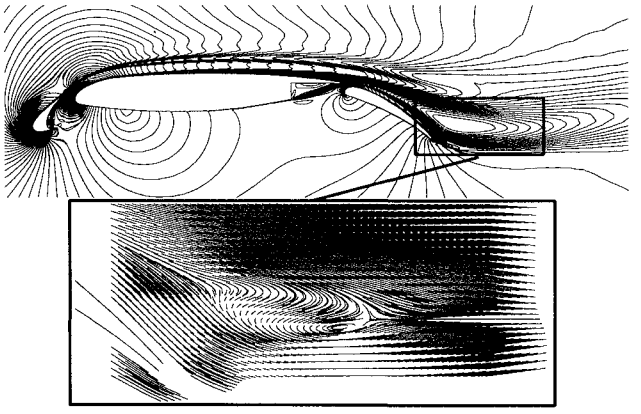

Fig. 14 Velocity magnitude contours and particle traces for the k-ω solution at 23.4-deg angle of attack.

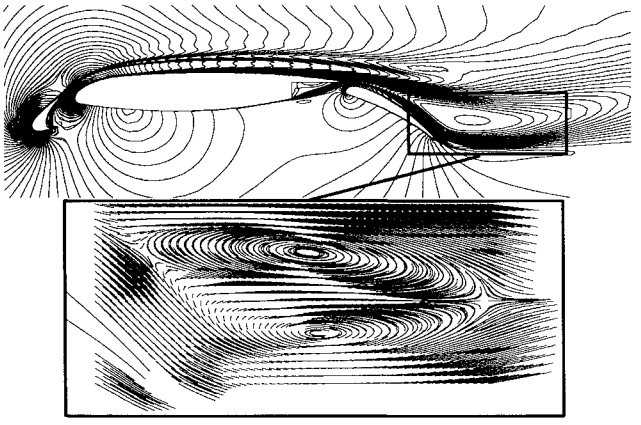

Fig. 15 Velocity magnitude contours and particle traces for the k-ω solution at 25.0-deg angle of attack.

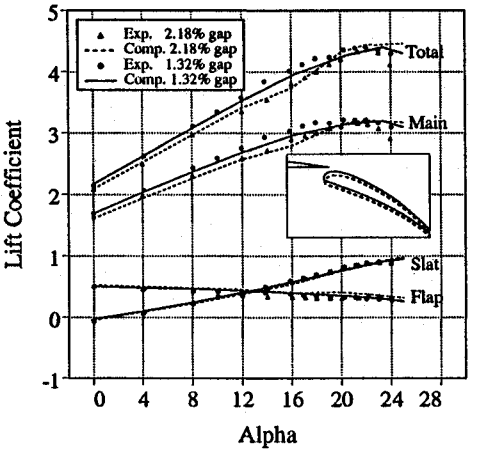

Fig. 16 Lift coefficient vs angle of attack comparing results from two different flap gaps.

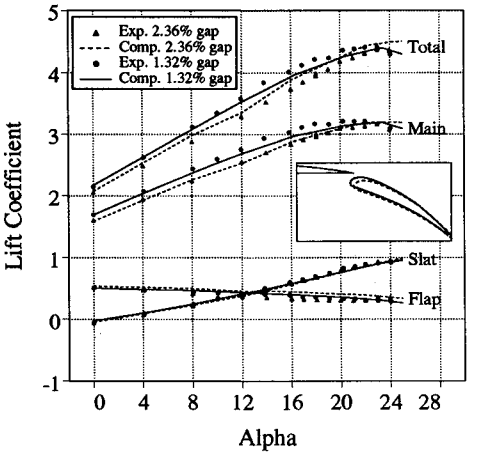

Fig. 17 Lift coefficient vs angle of attack comparing results from two different flap gaps.

particle traces in the aft region of the flowfield above the flap. Figure 14 shows results at 23.4 deg, and Fig. 15 plots the 25.0-deg angle-of-attack results. These plots show how the wake of the main element convects directly over the top of the flap surface and spreads rapidly as it encounters the adverse pressure gradient and flow curvature. This causes a dramatic deceleration of the fluid, which at these angles of attack is enough to cause the flow to reverse. The growth of this off-body separation corresponds to the loss of lift encountered at an angle of attack of 25 deg. A close examination of the velocity magnitude contours in these two plots shows that the boundary layer on the aft upper surface of the main element is noticeably thicker at the higher angle of attack, and that downstream of this the jet of fluid between the slat and main-element wakes undergoes less curvature, indicating that the flow is losing circulation at angles of attack above maximum lift. Also, it is apparent in these plots that there is no boundary-layer separation present. This is typical of multielement configurations, that the flap only separates at the lower angles of attack because as the lift increases, the downwash from the slat and main elements causes an effectively lower angle of attack on the flap; this is why the lift curves show the flap unloading as the angle of attack increases.

Geometry Effects

A primary requirement for a design tool is to accurately predict the change in performance of a component due to changes in the geometry of the configuration. This is particularly true when designing multielement airfoils and trying to optimize the slat and flap gap and overhangs. An evaluation of the ability to predict such changes using the current scheme with the k-ω turbulence model and the finest grid density ($n4c4$) was undertaken by running two additional flap configurations for a range of angles of attack. Figure 16 shows the results of an increase in the flap gap from a value of 0.0132 chords to a value of 0.0218 chords. This first gap is the same configuration presented in all of the results above. The lift curves show that the computations have done a very effective job of quantifying the difference in lift at the angles of attack below 16 deg. Beyond this, the computations show too much lift for the larger gap, and too little lift for the smaller gap, and incorrectly predict a higher maximum lift for the larger gap configuration. Much of this lift error in the computations comes from the flap.

Figure 17 shows results from a comparison between the original configuration and a third configuration that has an increased flap gap of 0.0236 chords and also a flap overhang of 0.0025 decreased from the original overhang of 0.01 chords. Once again, the computations have done an excellent job of predicting the incremental lift loss at this flap setting for the lower angles of attack. But the prediction of maximum lift is off. Examination of the computational results for these two larger flap-gap cases show that the off-body separation does not occur until a higher angle of attack is reached compared to the smaller flap-gap case.

Reynolds Number Effects and Drag

Experimental evidence[30] shows that Reynolds number effects can be significant and that using experimental data from lower Reynolds number studies can lead to erroneous conclusions. Since the number of experimental facilities capable of operating at flight Reynolds numbers is limited, it will be

important for a computational tool to predict Reynolds number effects. In particular, the current three-element airfoil configuration was optimized at a Reynolds number of 9×10^6; Reynolds numbers above and below this condition result in lower maximum lift in the experimental study. Initial studies using the current computational method show qualitative agreement with this trend, but do not show the capability to reproduce the experimental maximum lift quantities reliably. This is not surprising given the sensitive nature of the maximum lift flow physics: a slight change in any of a large number of flow and/or computational parameters can make a significant difference in the maximum lift in both the computation and in the experiment. Further work is warranted to improve the ability to compute maximum lift.

The ability of the code to compute drag was also investigated. Both turbulence models agreed with the experimental results for drag coefficient at 0-deg angle of attack. However, at higher lift conditions, the computations predicted much greater quantities of drag than was reported in the experiment. This is not well understood at this time, except to say that this result is independent of the grid resolution. Further investigation of the drag computation is underway. One possible source for the discrepancy is the difference in the way that the drag was measured: the computational drag is the result of an integration of the pressure and skin-friction forces on the airfoil surfaces; the experimental values are determined by measuring the momentum loss in the wake of the airfoil.

Conclusions

A two-dimensional incompressible flow solver has been utilized to study the computational aspects of solving flow over high-lift airfoil configurations. A detailed grid study has provided guidelines for the grid densities required when utilizing both a one-equation Baldwin-Barth turbulence model and a two-equation k-ω turbulence model. The k-ω turbulence model does require more grid points than the Baldwin-Barth model, but it also outperforms the one-equation model. It is significantly better at computing maximum lift conditions and flap boundary-layer separation for a two-dimensional multielement airfoil, although it is not in perfect agreement with experimental results. It was shown that transition can effect the solutions at higher angles of attack. The multielement airfoil computations were performed for three different flap settings; the computations did an excellent job of predicting the lift at angles of attack below 16 deg for all three cases, but was able to accurately compute the maximum lift coefficient in only one case. The computations predicted a region of off-body separation in the wake of the main element at the highest angles of attack. Work is continuing in the development and evaluation of several turbulence models toward the goal of accurately predicting all the features of multielement airfoil flows.

Acknowledgments

This work would not have been possible without the helpful discussions and suggestions from numerous individuals at NASA Ames and members of industry. Special mention is given to Florian Menter for his development of the k-ω turbulence model used in this study.

References

[1]Meredith, P. T., "Viscous Phenomena Affecting High-Lift Systems and Suggestions for Future CFD Development," *High-Lift System Aerodynamics, 71st Fluid Dynamics Panel Meeting* (Banff, Alberta, Canada), Paper 19, 1993, pp. 19-1–19-8 (AGARD CP 515).

[2]Schuster, D. M., and Birckelbaw, L. D., "Numerical Computations of Viscous Flowfields About Multiple Component Airfoils," AIAA Paper 85-0167, Jan. 1985.

[3]Shima, E., "Numerical Analysis of Multiple Element High Lift Devices by Navier-Stokes Equations Using Implicit TVD Finite Volume Method," *Proceedings of the AIAA 6th Applied Aerodynamics Conference* (Williamsburg, VA), AIAA, Washington, DC, 1988, pp. 399–406 (AIAA Paper 88-2574).

[4]Chow, R., and Chu, K., "Navier-Stokes Solution for High-Lift Multielement Airfoil System with Flap Separation," AIAA Paper 91-1623, June 1991.

[5]Renze, K. J., Buning, P. G., and Rajagopalan, R. G., "A Comparative Study of Turbulence Models for Overset Grids," AIAA Paper 92-0437, Jan. 1992.

[6]Fritz, W., "Maximum and High-Lift Characteristics of Multi-Element Aerofoils," *High-Lift System Aerodynamics, 71st Fluid Dynamics Panel Meeting* (Banff, Alberta, Canada), Paper 5, 1993, pp. 5-1–5-12 (AGARD CP 515).

[7]Jasper, D., Agrawal, S., and Robinson, B. A., "Navier-Stokes Calculations on Multi-Element Airfoils Using a Chimera Based Solver," *High-Lift System Aerodynamics, 71st Fluid Dynamics Panel Meeting* (Banff, Alberta, Canada), Paper 8, 1993, pp. 8-1–8-11 (AGARD CP 515).

[8]Nelson, T. E., Zingg, D. W., and Johnston, G. W., "Numerical Solution of the Navier-Stokes Equations for High-Lift Configurations on Structured Composite Grids," *High-Lift System Aerodynamics, 71st Fluid Dynamics Panel Meeting* (Banff, Alberta, Canada), Paper 9, 1993, pp. 9-1–9-11 (AGARD CP 515).

[9]De Cock, K. M. J., "High-Lift System Analysis Using Unstructured Meshes," *High-Lift System Aerodynamics, 71st Fluid Dynamics Panel Meeting* (Banff, Alberta, Canada), Paper 12, 1993, pp. 12-1–12-20 (AGARD CP 515).

[10]Johnson, L. J., and Stolcis, L., "Prediction of the High-Lift Performance of Multi-Element Aerofoils Using an Unstructured Navier-Stokes Solver," *High-Lift System Aerodynamics, 71st Fluid Dynamics Panel Meeting* (Banff, Alberta, Canada), Paper 13, 1993, pp. 13-1–13-18 (AGARD CP 515).

[11]Bailey, R., Dimier, A., and Ronzheimer, A., "Application of Unstructured Grid Methods to 2D High-Lift Configurations," *High-Lift System Aerodynamics, 71st Fluid Dynamics Panel Meeting* (Banff, Alberta, Canada), Paper 14, 1993, pp. 14-1–14-13 (AGARD CP 515).

[12]Chow, R., Chu, K., and Carpenter, G., "Navier-Stokes Simulation of Flow Field Around a Blown-Flap High-Lift System," *High-Lift System Aerodynamics, 71st Fluid Dynamics Panel Meeting* (Banff, Alberta, Canada), Paper 15, 1993, pp. 15-1–15-10 (AGARD CP 515).

[13]Rogers, S. E., Wiltberger, N. L., and Kwak, D., "Efficient Simulation of Incompressible Viscous Flow over Single and Multielement Airfoils," *Journal of Aircraft*, Vol. 30, No. 5, 1993, pp. 736–743.

[14]Benek, J. A., Buning, P. G., and Steger, J. L., "A 3-D Chimera Grid Embedding Technique," *Proceedings of the AIAA 7th Computational Fluid Dynamics Conference* (Cincinnati, OH), AIAA, New York, 1985, pp. 322–331 (AIAA Paper 85-1523).

[15]Rogers, S. E., and Kwak, D., "An Upwind Differencing Scheme for the Steady-State Incompressible Navier-Stokes Equations," *Applied Numerical Mathematics*, Vol. 8, No. 1, 1991, pp. 43–64.

[16]Rogers, S. E., and Kwak, D., "An Upwind Differencing Scheme for the Time Accurate Incompressible Navier-Stokes Equations," AIAA Paper 88-2583, June 1988; also *AIAA Journal*, Vol. 28, No. 2, 1990, pp. 253–262.

[17]Rogers, S. E., Kwak, D., and Kiris, C., "Numerical Solution of the Incompressible Navier-Stokes Equations for Steady-State and Time-Dependent Problems," AIAA Paper 89-0463, Jan. 1989; also *AIAA Journal*, Vol. 29, No. 4, 1991, pp. 603–610.

[18]Chorin, A. J., "A Numerical Method for Solving Incompressible Viscous Flow Problems," *Journal of Computational Physics*, Vol. 2, No. 1, 1967, pp. 12–26.

[19]Roe, P. L., "Approximate Riemann Solvers, Parameter Vectors, and Difference Schemes," *Journal of Computational Physics*, Vol. 43, No. 2, 1981, pp. 357–372.

[20]Rogers, S. E., "On the Use of Implicit Line-Relaxation and Multi-Zonal Computations," *Proceedings of the AIAA 10th Computational Fluid Dynamics Conference* (Honolulu, HI), AIAA, Washington, DC, 1991, pp 953–954 (AIAA Paper 91-1611).

[21]Baldwin, B., and Barth, T., "A One-Equation Turbulence Transport Model for High Reynolds Number Wall-Bounded Flows," NASA TM 102847, Aug. 1990.

[22]Baldwin, B., and Barth, T., "A One-Equation Turbulence Transport Model for High Reynolds Number Wall-Bounded Flows," AIAA Paper 91-0610, Jan. 1991.

[23]Menter, F. R., "Improved Two-Equations Turbulence Models

for Aerodynamic Flows," NASA TM 103975, Nov. 1992.

[24]Wilcox, D. C., "Multiscale Model for Turbulent Flows," *AIAA Journal*, Vol. 26, No. 11, 1988, pp. 1311–1320.

[25]Menter, F. R., "Performance of Popular Turbulence Models for Attached and Separated Adverse Pressure Gradient Flows," AIAA Paper 91-1784, June 1991; also *AIAA Journal*, Vol. 30, No. 8, 1992, pp. 2066–2072.

[26]Menter, F. R., "Influence of Freestream Values on k-ω Turbulence Model Predictions," *AIAA Journal*, Vol. 30, No. 6, 1992, pp. 1657–1659.

[27]Jones, W. P., and Launder, B. E., "The Calculation of Low Reynolds Number Phenomena with a Two-Equation Model of Turbulence," *International Journal of Heat and Mass Transfer*, Vol. 16, No. 6, 1973, pp. 1119–1130.

[28]Wilcox, D. C., "The Remarkable Ability of Turbulence Model Equations to Describe Transition," *Proceedings of the 5th Symposium on Numerical and Physical Aspects of Aerodynamic Flows*, California State Univ., Long Beach, CA, 1992.

[29]Valarezo, W. O., Dominik, C. J., McGhee, R. J., Goodman, W. L., and Paschal, K. B., "Multi-Element Airfoil Optimization for Maximum Lift at High Reynolds Numbers," AIAA Paper 91-3332, Sept. 1991.

[30]Valarezo, W. O., Dominik, C. J., and McGhee, R. J., "Reynolds and Mach Number Effects on Multielement Airfoils," *Proceedings of the 5th Symposium on Numerical and Physical Aspects of Aerodynamic Flows*, California State Univ., Long Beach, CA, 1992.